The Astrophysical Journal, 956:32 (14pp), 2023 October 10 https://doi.org/10.3847/1538-4357/acf4fb

Standardized Luminosity of the Tip of the Red Giant Branch Utilizing Multiple Fields in NGC 4258 and the CATs Algorithm

Siyang Li[1], Adam G. Riess[1,2], Daniel Scolnic[3], Gagandeep S. Anand[2], Jiaxi Wu[3,4], Stefano Casertano[2], Wenlong Yuan[1], Rachael Beaton[2], and Richard I. Anderson[5]
[1] Department of Physics and Astronomy, Johns Hopkins University, Baltimore, MD 21218, USA; sli185@jh.edu
[2] Space Telescope Science Institute, Baltimore, MD 21218, USA
[3] Department of Physics, Duke University, Durham, NC 27708, USA
[4] Kuang Yaming Honors School, Nanjing University, Nanjing, Jiangsu 210023, People's Republic of China
[5] Institute of Physics, École Polytechnique Fédérale de Lausanne (EPFL), Observatoire de Sauverny, 1290 Versoix, Switzerland

Received 2023 June 15; revised 2023 August 24; accepted 2023 August 28; published 2023 October 5

Abstract

The tip of the red giant branch provides a luminous standard candle for calibrating distance ladders that reach Type Ia supernova (SN Ia) hosts. However, recent work reveals that tip measurements vary at the ~0.1 mag level for different stellar populations and locations within a host, which may lead to inconsistencies along the distance ladder. We pursue a calibration of the tip using 11 Hubble Space Telescope fields around the maser host, NGC 4258, that is consistent with SN Ia hosts by standardizing tip measurements via their contrast ratios. We find F814W-band tips that exhibit a full 0.3 mag range and 0.1 mag dispersion. We do not find any correlation between H I column density and the apparent tip to $0.04 \pm 0.03\ \mathrm{mag/cm^{-2}}$. We search for a tip–contrast relation (TCR) and measure the TCR within the fields of NGC 4258 of $-0.015 \pm 0.008\ \mathrm{mag}/R$, where R is the contrast ratio. This value is consistent with the TCR originally discovered in the GHOSTS sample of $-0.023 \pm 0.005\ \mathrm{mag}/R$. Combining these measurements, we find a global TCR of $-0.021 \pm 0.004\ \mathrm{mag}/R$ and a calibration of $M_I^{\mathrm{TRGB}} = -4.025 \pm 0.035 - (R - 4) \times 0.021$ mag. We also use stellar models to simulate single age and metallicity stellar populations with [Fe/H] from −2.0 to −0.7 and ages from 3 to 12 Gyr and reconstruct the global TCR found here to a factor of ~2. This work is combined in a companion analysis with tip measurements of nearby SN Ia hosts to measure H_0.

Unified Astronomy Thesaurus concepts: Red giant stars (1372); Standard candles (1563); Stellar distance (1595); Hubble constant (758); Observational cosmology (1146); Calibration (2179); Absolute magnitude (10); Luminosity function (942); Red giant tip (1371); Distance indicators (394)

1. Introduction

The tip of the red giant branch (TRGB) is a near-standard candle that forms as a consequence of the onset of helium burning in the degenerate cores of low-mass red giant stars (Serenelli et al. 2017). Because of its bright luminosity ($M_I \sim -4$ mag), the tip can be used to measure distances to galaxies beyond the Local Group (for instance, Lee et al. 1993; Radburn-Smith et al. 2011; Lee & Jang 2012; Tully et al. 2013; Jang & Lee 2017; Anand et al. 2021; Jang et al. 2021) and aid in the construction of extragalactic distance ladders to measure the Hubble constant, H_0 (Ferrarese et al. 2000; Freedman et al. 2001; Tammann et al. 2008; Mould & Sakai 2009; Hislop et al. 2011; Lee & Jang 2012, 2013; Tammann & Reindl 2013; Jang & Lee 2015; Freedman et al. 2019, 2020; Kim et al. 2020; Anand et al. 2022; Blakeslee et al. 2021; Anderson et al. 2023). It has been long known that the tip luminosity varies with color (Lee et al. 1993; Rizzi et al. 2007; Madore et al. 2009; Jang & Lee 2017; McQuinn et al. 2019), and its color-rectified luminosity or luminosity measured over a modest color range has been treated as a standard candle.

However, observations have revealed that measurements of the luminosity of the tip vary at the ~0.1 mag level in the I band even over a small, ~1 mag $V - I$ color range (for a compilation and discussion of recent measured luminosities with NGC 4258, Large Magellanic Cloud (LMC), and the Milky Way, see Blakeslee et al. 2021; Freedman 2021; Li et al. 2022). Strong evidence of this variation is anchored by LMC studies. Hoyt (2023) observed field-to-field variations of several tenths of a magnitude (after correction for extinction) accompanied by differences at the <0.03 mag level in the width of the Sobel responses of the luminosity function (LF). Similarly, Anderson et al. (2023) observed a 0.1 mag level difference in the tip of two subpopulations of red giants (those with small-scale variability in the A or B sequence) with 5σ confidence. Unfortunately, these metrics (width or variability) require very high signal-to-noise ratio (S/N) data that are not readily available for more distant hosts. They are also not measurable in the maser host, NGC 4258, which serves as perhaps the most important calibrator of the tip due to the ability to observe it with the same facilities and under similar conditions as Type Ia supernova (SN Ia) hosts.

Another measure that correlates with tip brightness, but which is feasible to measure in distant hosts, is the tip contrast ratio (the ratio of stars below and above the measured tip). Its relation with the tip has been observed at high (5σ) confidence by Wu et al. (2023) by comparing multiple halo pointings for several hosts in the GHOSTS sample, which can be attributed in part due to the measurement method itself. This property, largely driven by the presence of younger, asymptotic giant branch (AGB) stars more luminous than the tip, is expected to be related to characteristics of the stellar populations such as age and metallicity (Wu et al. 2023) based on the study of stellar isochrones. In analyses, it is essential that tip measurements are *standardized* to account for variations that arise from these stellar properties.

1.1. TRGB Measurements

Empirically, the tip is measured by locating the discontinuity in the number of stars along the giant branch LF, typically computed from inside a diagonal band placed on a color–magnitude diagram (CMD). This discontinuity can be located using edge-detection methods such as a Sobel filter (Lee et al. 1993; Sakai et al. 1996; Hatt et al. 2017, and references therein) or with a multiparameter model fit to the LF using least squares minimization (Wu et al. 2014) or maximum likelihood estimation (Méndez et al. 2002; Makarov et al. 2006; McQuinn et al. 2016; Kim et al. 2020; Li et al. 2022, and references therein). For the edge-detection approach, a filter, most often of the Sobel type, is evaluated across the LF to measure its weighted first derivative and identify the TRGB discontinuity (peak in the derivative function; Lee et al. 1993). However, this approach can result in several local maxima in the first derivative that are comparable in height or which are outside the "expected" range of tip values based on prior inferences. These effects can lead to a somewhat subjective differentiation between the true tip and spurious features. Previous measurements of the tip in NGC 4258 (such as Madore et al. 2009) involved supervision to decide which tip to accept and subjective definition of what area constitutes "the halo" (Jang et al. 2021). To address these issues, Wu et al. (2023) developed an unsupervised, Sobel-filter-based tip measurement algorithm as part of the Comparative Analysis of Tips (CATs) program and optimized its parameters to minimize the dispersion among multiple fields in Galaxy Halos, Outer disks, Star clusters, Thick disks, and Substructure (GHOSTS) survey (Radburn-Smith et al. 2011) galaxies. The CATs algorithm from Wu et al. (2023) differs from past tip measurement algorithms by using quantifiable, objective procedures that remove some of the subjective steps used in other work such as the choice of color band slopes and widths. It uses an entirely unsupervised Sobel-filter-based approach and accepts multiple tip measurements per population; this obviates the need to select a specific peak in the Sobel response, and accounts for variations in stellar properties that can produce tips of slightly different luminosities. The detections undergo a series of quality cuts that are applied in an unsupervised and consistent manner.

Wu et al. (2023) found that the measured tip magnitude becomes brighter with increasing contrast ratio, where the contrast ratio is defined as the quotient between the number of stars 0.5 mag fainter and brighter than the measured tip and may be related to properties of different stellar populations, LF characteristics, and measurement parameter choices that cause variations in the measured tip. We note that the exact origin of this relationship is inconsequential to the validity of its application as a calibrating tool in general (though the slope may change with smoothing and noise, see Sections 5 and 6). The tip–contrast ratio relationship can be used to standardize the tip so that distances to galaxies are calibrated in a more similar manner. When measuring the distance to a galaxy, the measured apparent magnitude tip should be tied to an absolute magnitude tip or zero-point that is calculated using a population of similar stellar properties, LF characteristics, and measurement parameter choices, otherwise the zero-point may not accurately reflect the true absolute magnitude of the tip of a population with those stellar properties and characteristics measured with a different setup. It will be important to investigate whether this relationship exists in other galaxies, especially those used to anchor the extragalactic distance ladder to measure H_0. NGC 4258 acts as an anchor galaxy for the TRGB-based distance ladder due to the availability of a geometric, maser-based distance (Reid et al. 2019; Pesce et al. 2020), and is an ideal testing ground for this hypothesis as multiple fields have been observed in the past (see Section 2).

In this study, we use the CATs algorithm to calibrate the tip–contrast ratio relationship in NGC 4258. We describe our data selection procedure in Section 2 and first provide an estimate of the average tip measured across all fields in NGC 4258, before any correction, in Section 3. We then calibrate the tip–contrast ratio relationship in Section 4. We recreate a tip–contrast ratio relationship with simulated populations in Section 5 and discuss our results in Section 6.

2. Data Selection

We retrieve all publicly available images of NGC 4258 in the approximate region of its halo (twenty-fifth mag isophote) that were taken in the Hubble Space Telescope (HST) ACS/WFC F814W, F555W, and F606W filters from the Mikulski Archive for Space Telescopes (MAST): GO-9477, PI: Madore (Madore 2002); GO-10399, PI: Greenhill (Greenhill 2004); GO-16198, PI: Riess (Riess et al. 2020); GO-16688, PI: Anderson (Anderson et al. 2021); and GO-16743, PI: Hoyt (Hoyt et al. 2021). We drizzle together overlapping fields that were taken in the same set of filters (F814W and F606W or F814W and F555W) and perform photometry using DOLPHOT (Dolphin 2002, 2016) and the same pipeline used in Anand et al. (2022). We apply the same set of DOLPHOT photometric quality cuts (crowd, sharp, object type, error flag, and S/N) for NGC 4258 from Anand et al. (2022), which are based on McQuinn et al. (2017), with the exception of the S/N F606W quality cut, which we set to $S/N = 3$ instead of $S/N = 2$. In Field 6 we note excessive error flagging by DOLPHOT of bright stars using the "benign" flag = 2 (a flag which according to the DOLPHOT manual is usable), which was not common in the other fields. Inspection of these stars indicated no issues we could identify for these stars. Rather than exclude them, we tested all other fields by measuring the difference in the TRGB for all other fields between error cutting and retaining error flag = 2 and found no significant difference. Indeed, the GHOSTS analyses (Wu et al. 2023) use all flag = 2 data. Therefore we concluded it was safe to retain the flag = 2 photometry for the field.

We find that the individual fields in Field 4 are clustered in three groups and can be better aligned if drizzled separately. We separate Field 4 into Group 1, Group 2, and Group 3, which we refer to as G1, G2, and G3, respectively. We show these groupings in Appendix A and ultimately do not use G3 or the bottom most field in our analysis because the stars are too sparse for us to find a proper alignment solution within DOLPHOT. The locations of the fields can be seen in Figure 1.

We provide a summary of the fields used in Table 1, and the photometry, along with other intermediate data products, used for this study in a publicly available GitHub repository[6] (Wu 2023).

---

[6] https://github.com/JiaxiWu1018/CATS-H0

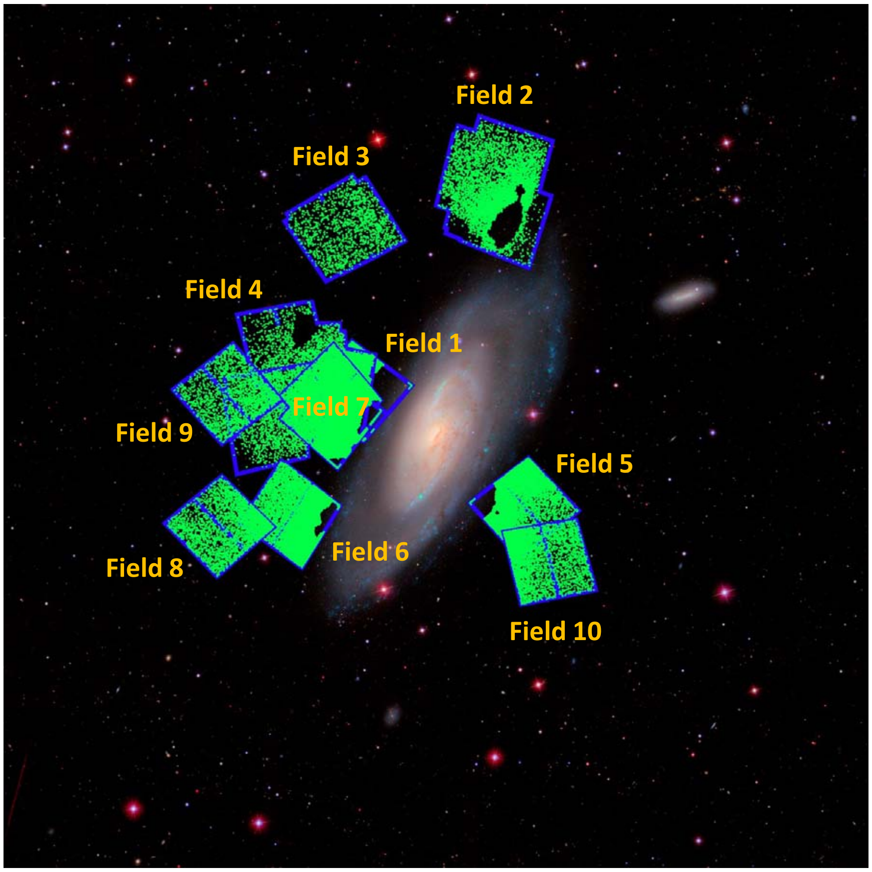

Figure 1. Footprints for the 10 fields (blue) and locations of stars that made it past the CATs spatial clipping algorithm (green). Field numbers are labeled in orange. The background image was created by combining *gri* images from the Sloan Digital Sky Survey (Alam et al. 2015). In this image, north and east correspond to the upward and leftward directions, respectively.

Table 1
Summary Table for the Fields Used in This Study

Field Number	Program	PI	Filters	Exposure Time (s)	
				F814W	F555W/F606W
1	GO-9477	Madore	F814W/F555W	2600	5700
2	GO-10399	Greenhill	F814W/F555W	1040	1300
3	GO-10399	Greenhill	F814W/F555W	1040	1300
4	GO-10399	Greenhill	F814W/F555W	1040	1300
5	GO-16198	Riess	F814W/F606W	640	785
6	GO-16198	Riess	F814W/F606W	640	785
7	GO-16688	Anderson	F814W/F606W	2250	2250
8	GO-16743	Hoyt	F814W/F606W	5146	5146
9	GO-16743	Hoyt	F814W/F606W	2614	5146
10	GO-16743	Hoyt	F814W/F606W	5146	5146

Note. Columns from left to right: field number, program numbers, principal investigators, filter sets, and exposure times for each filter.

3. Tip Properties in NGC 4258

It is useful to examine the direct tip measurements and properties first before applying any additional corrections. To measure the tip, we use the same algorithm from Wu et al. (2023). This algorithm applies spatial clipping to remove contamination from young stars, optimizes a color band, smooths the LF within the optimized color band with Gaussian-windowed, Locally Weighted Scatterplot Smoothing (GLOESS) with a smoothing parameter of $s = 0.1$, applies a weighted Sobel filter to obtain edge-detection responses (EDRs), and finds the tip based on local inflection points along the LF. The detected tips and EDRs using a smoothing parameter of $s = 0.1$ near the RGB among the 11 different fields around NGC 4258 are shown in Figure 2 and compared in Figure 3. They appear quite inhomogeneous even after we reject tips with contrast ratios less than 2; we find that these latter detections have high levels of noise due to a weakly defined break and in many cases correspond to the tip of the AGB rather than the RGB.

The range of detected tips is several tenths of a magnitude. The average of the 11 field tips is $\mathrm{F814W}_0 = 25.37$ mag with a dispersion of 0.099 mag. This value uses the external extinction

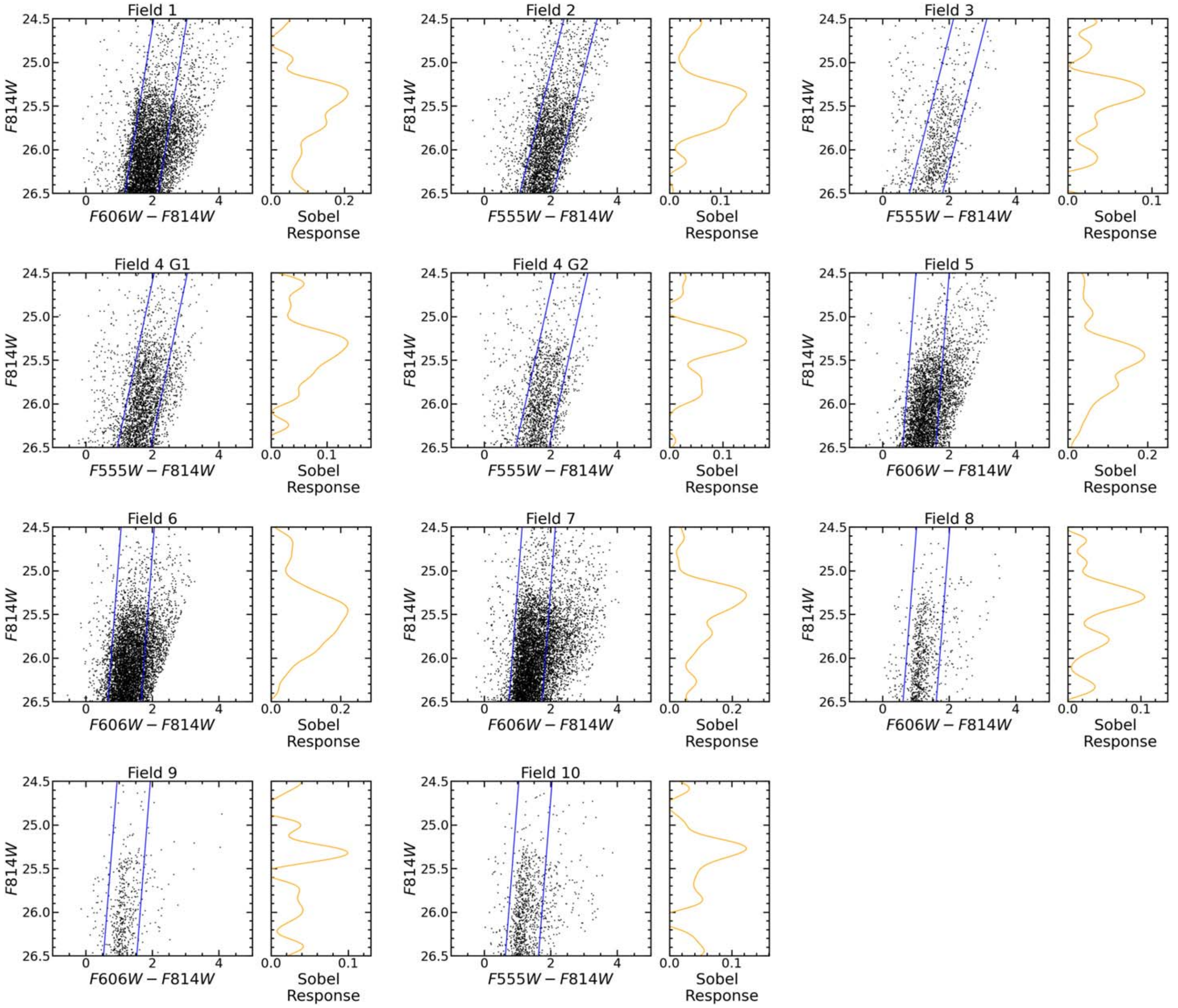
Field 1
Field 2
Field 3
Field 4 G1
Field 4 G2
Field 5
Field 6
Field 7
Field 8
Field 9
Field 10

Figure 2. CMDs after applying quality and spatial cuts for the fields analyzed in this study are shown in the left panels of each subplot. Internal and external extinction corrections have not yet been applied in this plot. Diagonal blue lines in the left panels for each subplot indicate the optimized color band determined with the CATs algorithm, and the orange lines in the right panels for each subplot show the Sobel response generated with the CATs algorithm with a smoothing parameter of 0.1 and stars within the blue color bands.

estimate of 0.030 mag from Schlafly & Finkbeiner (2011) and $A_{\mathrm{F814W}}/E(B-V)=2.107$ (R. Anderson 2023, private communication), consistent with Anderson et al. (2023), but is not corrected for internal extinction (Anderson 2022), which has an expected average $A_{\mathrm{F814W}}=0.013$ mag using Ménard et al. (2010; see Wu et al. 2023 for a discussion). For two cases, Fields 1 and 5, we computed their value by averaging rather than selecting one of two tips.

If instead we average the fields by the number of stars below the tip each contains (hence weighted by the inverse Poisson error as though together they were one big field) we find $\mathrm{F814W}_0=25.42$ mag, where we present this average in the context that a change in methodology can significantly affect the result. It is important to note here that the field dispersion of $\sigma=0.10$ mag dominates the statistical bootstrap precision of $<$0.03 mag per field. This dispersion cannot be attributed to disk contamination due to our use of spatial masking or the small number of younger stars that remain after spatial clipping in the corners of the fields (for instance, with Fields 1 and 5). We also note that none of these fields are outliers (more than 2σ from the mean, full range of 25.27–25.61 mag). Because of this field-to-field variation, the simple mean tip of NGC 4258 is no more accurate than $\sigma\sim0.03$ mag. We also note that our results are in good agreement with the tip measurements in different fields used by Jang et al. (2021) and Anand et al. (2022).

With the maser distance, the simple means result in $M_{\mathrm{F814W},0}=-4.05\pm0.03$ mag, or $M_{\mathrm{F814W},0}=-4.00\pm0.03$ weighted by star number, which serves as a useful reference for studies of the metal-poor tip which do not embark on further standardization. We provide the measured tips, uncertainties, contrast ratios, tip–contrast relation (TCR)-corrected tips, internal extinction, and foreground extinction values in

Table 2
Summary of Measured TRGB Parameters

Field	$m^{R=4}_{\rm F814W,TRGB}$	$\sigma_{\rm TRGB}$[a]	R	$N_{+,1.0}$	$m^{\rm TRGB}_{\rm F814W}$	A_I(Int.)	A_I(MW)
1	25.375	0.041	7.00	3193	25.360	0.019	0.03
1	25.619	0.462	2.91	4529	25.690	0.019	0.03
2	25.332	0.108	4.42	1971	25.367	0.014	0.03
3	25.301	0.130	4.38	480	25.334	0.011	0.03
4 G1	25.291	0.048	5.41	1386	25.304	0.013	0.03
4 G2	25.296	0.041	6.35	902	25.288	0.012	0.03
5	25.453	0.041	6.75	2451	25.441	0.016	0.03
5	25.707	0.567	2.64	3199	25.781	0.016	0.03
6	25.468	0.041	6.38	4120	25.462	0.014	0.03
7	25.306	0.041	7.46	3550	25.280	0.016	0.03
8	25.331	0.041	7.25	474	25.302	0.010	0.03
9	25.330	0.041	6.29	302	25.320	0.009	0.03
10	25.382	0.040	11.41	531	25.268	0.011	0.03

Note.

[a] From Equation (1). From left to right: field number, tip corrected to a fiducial contrast ratio of $R = 4$, tip errors, contrast ratios, number of stars one magnitude fainter than the measured tip, original tips before TCR correction, internal extinction estimated with Ménard et al. (2010), and Milky Way extinctions estimated with Schlafly & Finkbeiner (2011). Tip, error, and contrast ratios were measured using the unsupervised CATs algorithm. The tips shown in the fifth column from the left have not been corrected for internal and foreground extinction.

Table 2. We also explore more tip measurement properties in Appendix B.

4. Tip–Contrast Ratio Relationship

It is not entirely clear what produces the large variance of EDRs shown in the fields of NGC 4258, and changing the level of smoothing changes the magnitude of the variance (see also Anderson et al. 2023). However, to reduce the bias due to a mismatch when they are used to calibrate the TRGB in other fields (e.g., in SN Ia hosts), we seek to standardize or homogenize the tip measurements across different fields. Color has been used (Rizzi et al. 2007; Jang & Lee 2017) for fields where the TRGB has been measured over a wide color range. However, the variance we see is present after selecting a narrow color range ($\Delta V - I \sim 1.0$). Here we follow the approach of Wu et al. (2023) who found an empirical relation between the observed tip magnitude of a field and the measured contrast ratio (the ratio of stars above versus below the tip, parameterized as R).

We characterize and employ the empirically determined relation between the brightness of the tip and the contrast ratio. We measure the tips and contrast ratios for the 11 fields described in Section 2 and present them in Table 2. For fields with more than one tip, we average the tips measured with CATs in each field (weighted by their contrast ratios), correct for internal and foreground extinction, and plot these values in the top panel of Figure 4. Tip uncertainties were estimated using the model determined in Wu et al. (2023):

$$\sigma = \sqrt{\left[\left(\frac{2e^{1.5(3-R)}}{e^{1.5(3-R)}+1}\right)\left(\frac{1}{N_{+,1.0}-100}\right)^{0.1}\right]^2 + 0.04^2}\ \text{mag}. \tag{1}$$

We look for a relationship of the form:

$$m^{R=4}_{\rm TRGB} = m_{\rm TRGB} - (R - 4.0) \times m, \tag{2}$$

where $m^{R\,=\,4}_{\rm TRGB}$ is the fiducial tip at a contrast ratio of 4, $m_{\rm TRGB}$ is the measured tip before correction, R is the contrast ratio, and m is the slope of the tip–contrast ratio relationship. We first determine m via a linear least squares regression to the measured tips in Table 2, and find $m = -0.015 \pm 0.008$ mag/R. We do not find any outliers outside a 3σ clip. This value is 1σ from the calibration by Wu et al. (2023) of -0.023 ± 0.005 mag/R. A weighted average of these two measurements yields -0.021 ± 0.004 mag/R. Following Equation (2), we then measure a tip at a contrast ratio of 4 of $m^{R=4}_{\rm F814W} = 25.361 \pm 0.0136$ mag. We subtract the maser distance of $\mu_{\rm N4258} = 29.397 \pm 0.0324$ mag from Pesce et al. (2020) to find a zero-point of:

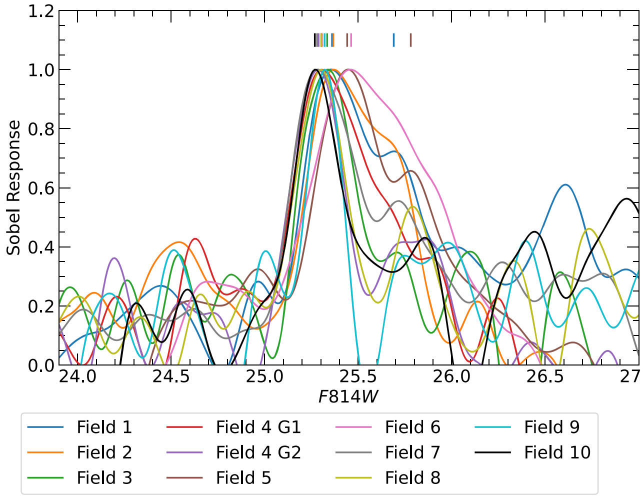

Figure 3. Normalized Sobel responses for all fields described in Section 2 overlaid for comparison. The plotted lines here are identical to the orange lines in Figure 2 and produced using the CATs algorithm. We measure these Sobel responses for each field using the CATs algorithm by first applying spatial clipping, optimizing a color band selection, applying 0.1 smoothing to the LF, and evaluate the Sobel response using the same procedure from Wu et al. (2023). The Sobel responses shown here have not yet been corrected for internal or external extinction. We mark the locations of the measured TRGB from these Sobel responses with tick marks colored with their corresponding Sobel response curve at the top of the figure.

Table 3
Summary of Tip Measurements from Sections 3 and 4

Method	$m_{\rm F814W}^{\rm TRGB}$	MW $A_{\rm F814W}$	Int. $A_{\rm F814W}$	TCR
Average (by field)	25.37	0.030	Not applied	None
Average (by stars)	25.42	0.030	Not applied	None
Standardization	25.372 ± 0.0136	0.030	Not applied	−0.021 ± 0.004
Standardization	25.361 ± 0.0136	0.030	0.011	−0.021 ± 0.004

Note. The standardized tip is taken to be at a fiducial contrast ratio of $R = 4$. For the tip measurements shown here, we applied foreground extinction correction but not internal extinction to facilitate better comparison to past studies in the literature.

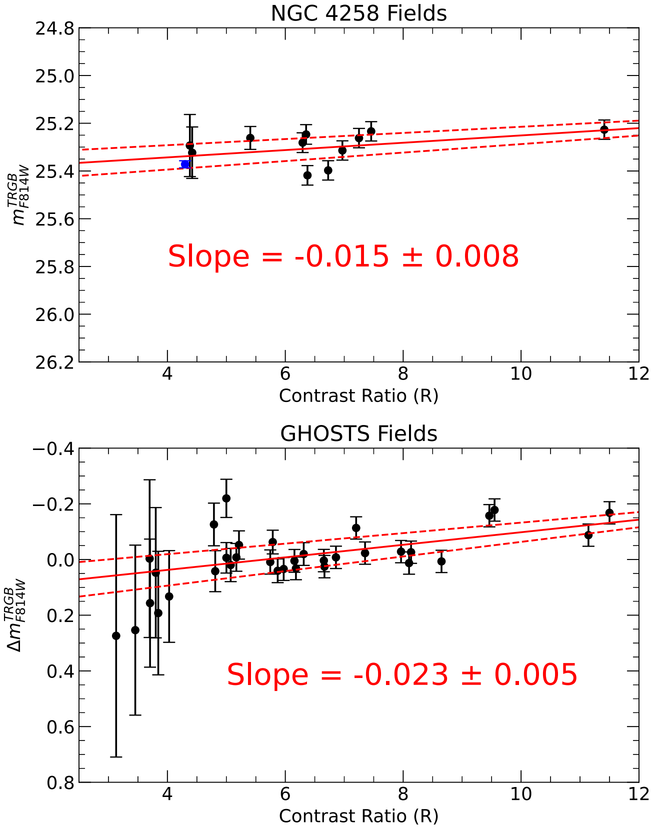

Figure 4. Measured tips as a function of contrast ratio using the CATs algorithm described in Wu et al. (2023) using the NGC 4258 fields from Figure 1 and Table 1 (top) and the GHOSTS fields (Radburn-Smith et al. 2011; bottom). An approximated tip–contrast ratio pair from Figure 10 in Jang et al. (2021) is added in the top panel in blue for comparison purposes only. We note that their measurement setup would likely produce a TCR different from the one calibrated here.

$$M_{\rm F814W}^{R=4} = -4.036 \pm 0.035\ {\rm mag} - (R-4)\times 0.021. \quad (3)$$

Removing the internal extinction correction gives $m_{\rm F814W}^{R=4} = 25.372 \pm 0.0136$ mag and a zero-point of:

$$M_{\rm F814W}^{R=4} = -4.025 \pm 0.035\ {\rm mag} - (R-4)\times 0.021. \quad (4)$$

We summarize the mean and standardized tips across all fields from Section 3 and this section in Table 3.

4.1. H I Regions

We examine whether the tip measurements correlate with the amount of H I present in each field. We obtain H I column density measurements from Heald et al. (2011). In the left panel of Figure 5, we overlay the field contours on the H I map from Heald et al. (2011). In the right panel of Figure 5, we plot the TCR-corrected tips from Table 2 as a function of the mean H I column density for each field using the H I map. We plot a horizontal red line at 25.37 mag for reference, which corresponds to the TCR-corrected tip from Section 4. We fit the points in Figure 5 with a linear least squares regression and find a slope of 0.04 ± 0.03 mag cm^{-2}. We do not find a significant trend (i.e., $<1.5\sigma$) between the H I column densities and measured tips after applying the CATs algorithm and TCR correction. If we add back in stars that were removed with spatial clipping, we find a fit of 0.05 ± 0.03 mag cm^{-2}.

5. TCR Simulations

In this section, we investigate whether a tip–contrast ratio relationship can be created using the CATs algorithm applied to simulated stellar populations. To do this, we use ArtPop, which is a Python package that can generate synthetic stellar populations and artificial images of stellar systems (Greco & Danieli 2022) using Modules for Experiments in Stellar Astrophysics (MESA; Paxton et al. 2011, 2013, 2015) and Isochrones and Stellar Tracts (MIST; Choi et al. 2016; Dotter 2016). While these simulations include noise due to interpolation errors and choices of stellar models, we attempt to reproduce a TCR in general within the limitations of the single age and metallicity synthetic populations using informed assumptions about the underlying populations. We do not necessarily attempt to recreate a population of stars in a halo field.

We simulate a grid of stellar populations of single ages and metallicities from 3 to 12 Gyr and [Fe/H] from −2 to −0.7 (see Figure 6). The total mass for each population is $6 \times 10^9\ M_\odot$. To reflect actual measurement conditions better, we add Gaussian distributed noise following an exponential model of $\sigma = Ae^{Bm}$ where σ is the noise and m is the magnitude of the star. We calculate the parameters A and B by fitting the uncertainties estimated using artificial stars for NGC 1448 from the Extragalactic Distance Database (EDD; Tully et al. 2009; Anand et al. 2021). We selected NGC 1448 as a representative galaxy to use for galaxies used to measure H_0 in a companion study (Scolnic et al. 2023). For $\sigma_{\rm F606W}$ and $\sigma_{\rm F814W}$, we find $A = 1$ and $B = 0.710$, and $A = 1.684$ and $B = 0.721$, respectively. Because NGC 1448 is at a different distance than NGC 4258, we apply an additional scaling so that the errors are 0.05 mag at F814W = −4 mag and F606W = −3 mag, which we take to be approximately the location of the tip. Then, we use the CATs algorithm with the baseline parameters described in Section 4 to measure the tip and contrast ratio for each simulated population of stars.

We first plot the measured tips and contrast ratios in Figure 7. We limit the range of interest to contrast ratios

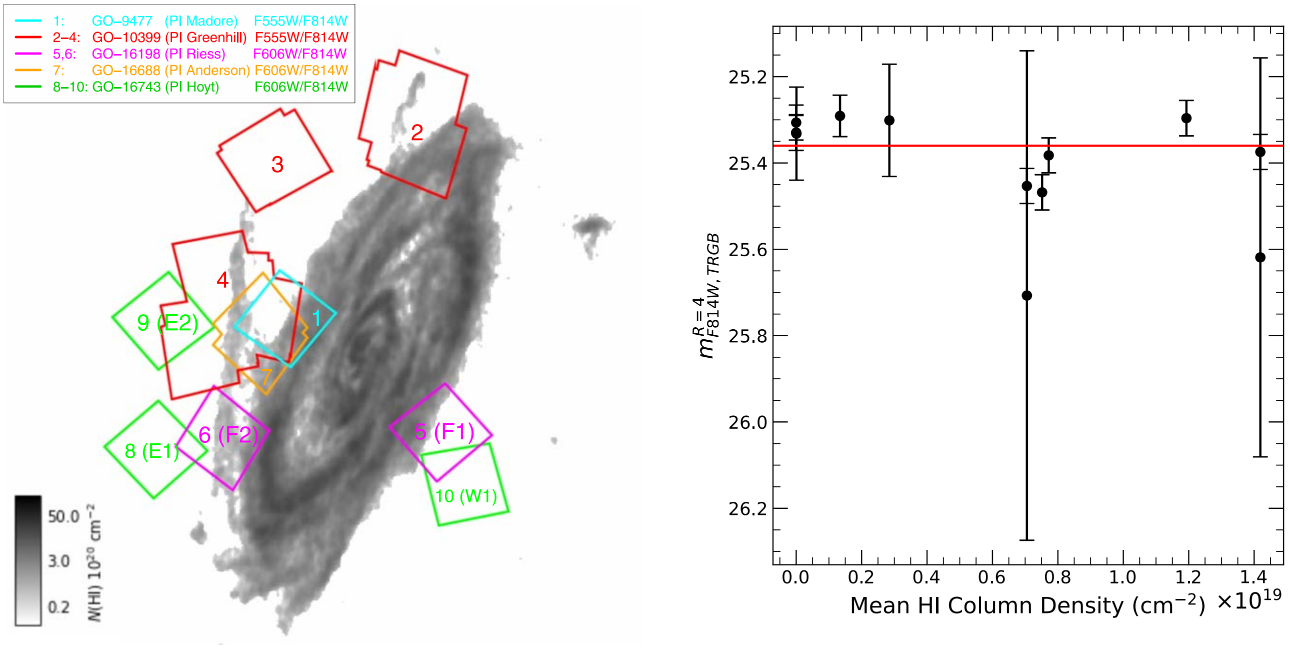

Figure 5. Left: locations of the 10 fields analyzed in this study overplotted on an H I density map from Heald et al. (2011). Right: TCR-corrected tips from Table 2 as a function of the mean H I column density. We do not find a significant trend between the corrected tips and H I column densities.

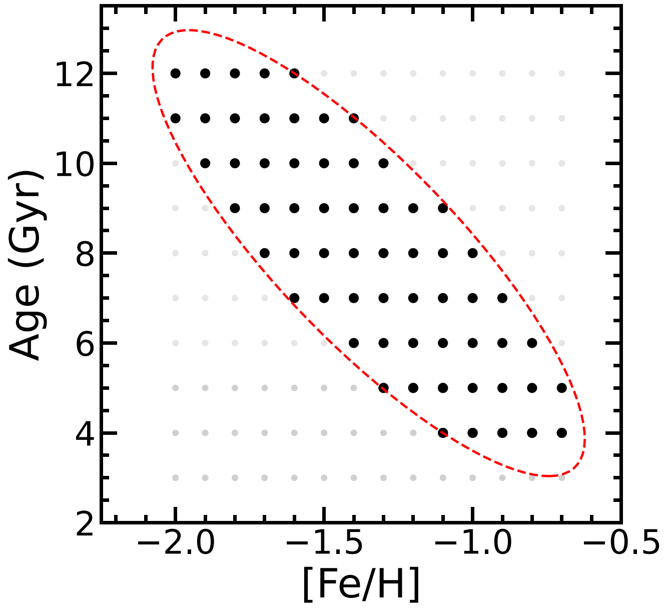

Figure 6. Grid of ages (3–12 Gyr) and metallicities ([Fe/H]; −2 to −0.7) used to simulate stellar populations for Figure 7. To approximate an old, metal-poor to young, metal-rich trend, we draw an ellipse along this axis on the plot. Points that fall inside this ellipse are shown as large, solid dots while points that lie outside this ellipse are shown as smaller fainter dots.

between 3 and 12 to match more closely the contrast ratios observed in NGC 4258 and for GHOSTS galaxies from Wu et al. (2023). We note that not all age and metallicity combinations plotted may exist in nature, and real halos are not simple populations. To select a more realistic sample, we draw an ellipse roughly containing populations that follow old and metal-poor to young and more metal-rich. We show this selection in Figure 6 and plot points that lie inside the ellipse in both Figures 7 and 6 as large, solid dots. Points that lie outside the ellipse are shown as lighter, smaller dots. For instance, 3 Gyr populations may be too young for stars to reach the tip (Serenelli et al. 2017), which is why they are excluded from the ellipse.

To measure the slope for the large, solid points, we apply an unweighted linear least squares fit and find a slope of -0.010 ± 0.002 mag$/R$. Similar to the empirical calibration found in Section 4, we find a significant inverse relationship between the tip magnitude and contrast ratio (i.e., the tip magnitude becomes brighter with increasing contrast ratio). This fit corresponds to the center subplot in Figure 7. We note that the most of the slopes found in these simulations agree well with those found empirically in Equations (3) and (4) and that these simulations use stellar populations of single ages and metallicities, while the stellar populations used for the empirical measurements contain a mixture of ages and metallicities.

5.1. *Impact of Smoothing*

To understand better the impact of the measurement technique itself on the TCR, we repeat the procedure described above with a grid of values for smoothing and noise. We apply (1) GLOESS smoothing values of $s = 0.05$, 0.10, and 0.15; (2) noise values of 0.02, 0.05, and 0.10 mag to all simulated magnitudes; and (3) the same age and metallicity range as used above. We fit the points with a linear least squares regression and plot the results in Figure 7. We find that in general, the fitted slopes increase in steepness with increasing smoothing and noise, although this trend could vary with different LFs (see Anderson et al. 2023). We notice that the smoothing function with a large smoothing of 0.15 attempts to smooth out the tip discontinuity. This results in a smoothed LF with a larger number of stars brighter than the tip when compared to a smoothed LF using a lower smoothing parameter. This occurs despite the bins in the unsmoothed LF remaining the same. We describe this effect in further detail in Appendix C.

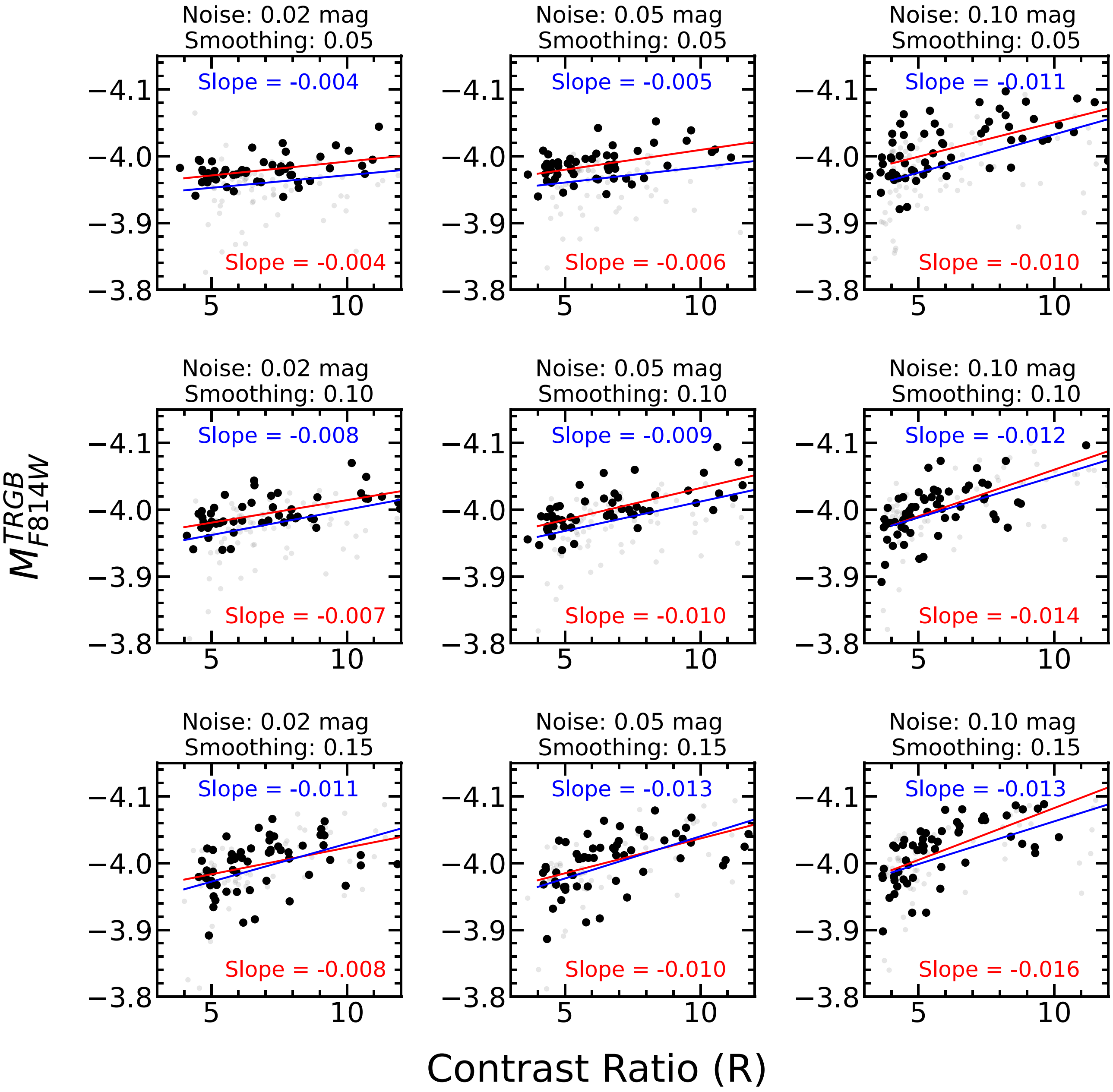

Figure 7. Tip measurements as a function of contrast ratio using the CATs algorithm on simulated populations of single ages (3–12 Gyr) and metallicities ([Fe/H]; −2 to −0.7) generated with ArtPop with the selection shown in Figure 6. We then apply the CATs algorithm to this grid of simulated populations with a grid of noise (0.02, 0.05, and 0.10 mag) and smoothing values (0.05, 0.10, and 0.15). Noise values are added using the exponential model of $\sigma = Ae^{Bm}$, where the coefficients are provided in Section 5. We restrict and fit each subplot to contrast ratios between 3 and 12. We also restrict the tips to be fainter than −4.1 mag as we find tips brighter than this often correspond to the tip of the AGB rather than TRGB. We show the points that have ages and metallicities that lie inside the ellipse from Figure 6 as large, solid black dots and points with ages and metallicities that lie outside the ellipse as smaller, fainter dots. Linear least squares fits and their slopes are shown in red (large dots) and blue (all dots including large and small). The fits are unweighted.

These populations are generated using homogeneous ages and metallicities, whereas observed fields will likely contain a mixture of different stellar properties. We note that we do not attempt to reproduce the observed halo fields, as creating a simulated population that accurately reflects the possible mixtures of stellar properties involves detailed considerations that are outside the scope of this study. In addition, simulations can also include additional errors due to interpolation and variations in the models. However, this independent replication of the tip–contrast ratio relationship using simulated populations suggests the tip–contrast ratio relationship is not an artifact of field placement and can be impacted by smoothing and noise.

6. Discussion

We calibrated the tip–contrast ratio relationship in NGC 4258 and provide a standardized tip zero-point at a fiducial contrast ratio of 4 that can be used to anchor extragalactic distance measurements. We generated simulated populations using ArtPop (Greco & Danieli 2022) and reproduced a tip–contrast ratio relationship with the CATs algorithm demonstrating that the tip–contrast ratio relation not originate from field placement and is impacted by noise and smoothing.

We investigated the potential effects of H I column density on our results. Jang et al. (2021) and Anand et al. (2022) argue that H I regions may affect the measured tip by contaminating the sample with nonnegligible internal extinction and younger stars in the halo. However, Wu et al. (2023) argues that the results from Ménard et al. (2010) demonstrate that extinction in the halo where the tip is typically measured is negligible, even in the presence of H I gas. In our analysis, we remove younger stars using the spatial clipping process described in Wu et al. (2023), which was based on the concepts from Anand et al. (2018, 2022).

We do not find evidence of a significant relationship between the measured tip and amount of H I gas present in the field after spatial clipping. This suggests that the measurement presented above is not affected by the trend observed between the measured tip and H I column density described in Beaton et al. (2018), Anand et al. (2022), and Jang et al. (2021). We note that even if there was a remaining relationship between H I column density and the tip, the low uncertainty of 0.005–0.008 mag$/R$ in the fitted tip–contrast ratio slope presented in Section 4 suggests that any effects from measuring the tip using stars in H I regions, even if remaining, is well accounted for in the fitted tip–contrast ratio relationship to the degree that the fields are positioned similarly to those used here. We also note that SN Ia hosts do not have H I maps available or have H I maps that lack sufficient resolution (SN hosts ~ 20 Mpc; see Condon 1987; Condon et al. 1996). Spatial clipping is a method that can remove contamination from younger stars that can be applied to both anchors and host galaxies as opposed to direct removal of H I regions via H I maps.

The tip–contrast ratio relationship represents an approach that is distinct but consistent with previous measurements of the tip and can be used to explain the large ($\sim$0.1 mag) spread in recent tip zero-point calibrations (see Blakeslee et al. 2021; Freedman 2021; Li et al. 2022). Instead of assuming that a single, universal tip zero-point that can be used with any stellar population regardless of its composition of different stellar and LF properties or measurement setup, we standardize the tip and its zero-point to account for the variations due to these astrophysical properties and measurement parameters such as age and smoothing. This interpretation also means that multiple tip discontinuities can exist in a single LF, as fields with mixtures of stars with different stellar properties can have multiple subpopulations that exhibit a slightly different tip, though detecting these peaks will depend on the relative distance between the peaks and the degree of smoothing and noise. Previous measurements of the tip often selected a single tip discontinuity over others or proximity to an accepted range of tips based on previous studies and required supervision to determine which peak to choose that rejects certain tips in favor of others. We discuss an example of this in Appendix D. The CATs algorithm used in this study is unsupervised to avoid this potential subjective bias.

We hypothesize the TCR relationship originates from a combination of astrophysical and measurement processes such as age, metallicity, photometric errors, and smoothing. Observationally, we find that the tip varies with the contrast ratio similar to the trends found in Anderson et al. (2023) for the LMC and Wu et al. (2023) for GHOSTS galaxies and argue that a given tip zero-point should be used to calibrate tip measurements of similar characteristics. Even if the TCR were entirely due to a particular choice of measurement setup and has no astrophysical origin, or vice versa, it does not change the fact that there is an observable variation in the tip against a parameter, the contrast ratio, that was previously not accounted for and that this variation should be accounted for in future measurements involving the tip to ensure greater consistency when using the tip to measure distances. There may be an additional uncertainty that will need to be propagated into distance measurements due to a change in the slope of the TCR due to different photometric noise in different galaxies. We plan to investigate this topic in further detail and note that this does not change the results presented in this paper, which calibrates the TCR in a single galaxy.

The tip currently plays an important role in the "Hubble tension" debate as it can be used to measure H_0 independently and parallel to the Cepheid distance scale. It will be essential to measure the TRGB-based H_0 using this improved standardization to increase the accuracy of future extragalactic distance measurements. We present this work in a companion paper in Scolnic et al. (2023).

Acknowledgments

S.L. is supported by the National Science Foundation Graduate Research Fellowship Program. D.S. is supported by Department of Energy grant DE-SC0010007, the David and Lucile Packard Foundation, the Templeton Foundation, and the Sloan Foundation. R.I.A. is funded by the SNSF through an Eccellenza Professorial Fellowship, grant No. PCEFP2_194638. R.L.B. acknowledges support from NSF-AST 2108616.

This research has made use of NASA's Astrophysics Data System and is based on observations made with the NASA/ESA Hubble Space Telescope obtained from the Space Telescope Science Institute, which is operated by the Association of Universities for Research in Astronomy, Inc., under NASA contract NAS 5-26555. These observations are associated with programs 9477, 10399, 16198, 16688, and 16743.

Some of the data presented in this paper were obtained from the Mikulski Archive for Space Telescopes (MAST) at the Space Telescope Science Institute. The specific observations analyzed can be accessed via doi:10.17909/6w5y-hh50.

Data Availability

The data and CATs algorithm used for this analysis can be found on GitHub: https://github.com/JiaxiWu1018/CATS-H0 and on Zenodo at doi:10.5281/zenodo.8271583. We encourage the community to reproduce and provide feedback on this analysis.

Appendix A
Field 4 Groups

We show the positions of the three groups that make up Field 4 in Figure 8.

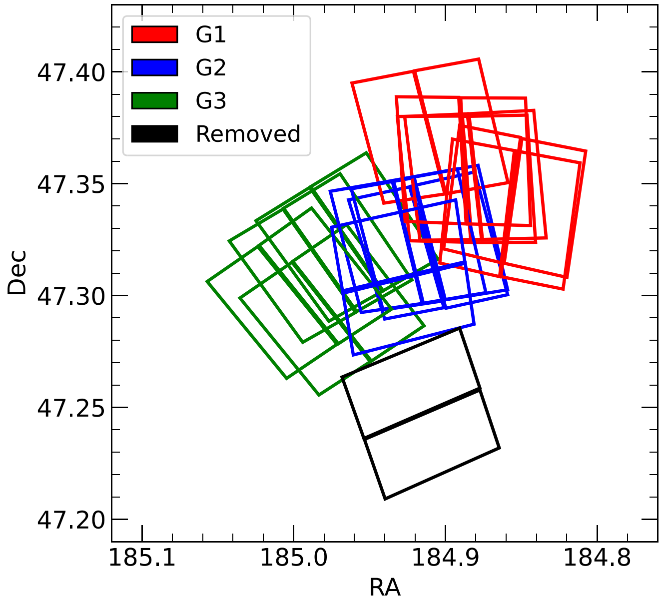

Figure 8. Grouping of the three G fields for Field 4. We remove the fields colored in black and green; Field 4 comprises only the fields colored in blue and red. In our analysis we measure the tip separately for G1 and G2.

Appendix B
Measuring Tips

The CATs algorithm (Wu et al. 2023) measures the spatial density of blue stars and masks high-density regions to remove young-star contamination (a step called spatial clipping). It then selects a diagonal region in the CMD of fixed width and variable slope and position to maximize the number of RGB stars contained within that region. Finally, it bins and smooths the LF consisting of red giants and asymptotic giants. We plot the CMDs for the 10 fields analyzed in this study after the photometric quality cuts and spatial cuts in Figure 2, which also shows the diagonal regions selected to measure the LFs.

The LFs appear rather fuzzy near the visual tip of the TRGB. Smoothing and weighting are necessary to evaluate the derivative of such noisy data. However, we note that various options used to smooth and weight the derivative will generate a bias in the determination of its position, even without noise, due to the asymmetric shape of the LF. This is illustrated in Figure 9 where we show several common choices.

In Figure 9, we simulate an LF with 1,000,000 samples using von Neumann rejection sampling and the broken-power-law model described in Méndez et al. (2002), Makarov et al. (2006), and Li et al. (2022) using realistic model parameters of $m_{\mathrm{TRGB}} = -4$ mag and $\alpha = \beta = \gamma = 0.3$, where α, β, and γ correspond to a, b, and c in Makarov et al. (2006), respectively. We Gaussian (GLOESS) smooth the LF at values of $s = 0.01$, 0.05, 0.1, and 0.15 and evaluate the derivative of the LF with three choices of functions with different weights or normalizations:

S/N EDR (Górski et al. 2018; Wu et al. 2023):

$$\mathrm{EDR}(i) = \frac{N(i+1) - N(i-1)}{\sqrt{N(i+1) + N(i-1)}}. \tag{B1}$$

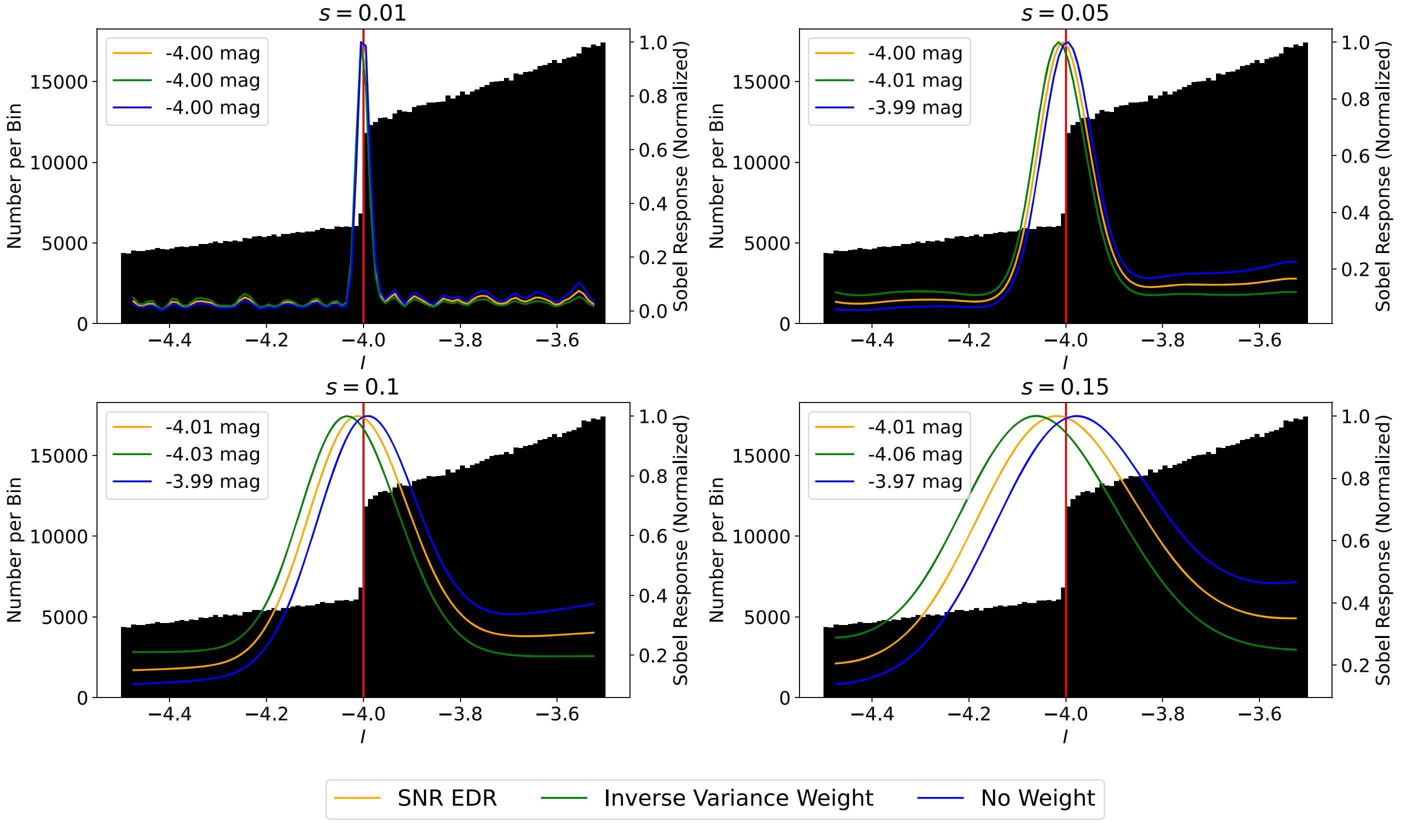

Figure 9. Sobel responses with four smoothings ($s = 0.01$ (top left), 0.05 (top right), 0.1 (bottom left), and 0.15 (bottom right)) and three different weightings (CATs (orange; Equation (B1)), inverse variance (green; Equation (B2)), and none (blue)) on the same LF simulated with 1,000,000 samples using von Neumann rejection sampling, a TRGB at −4 mag, and shape parameters of $\alpha = \beta = \gamma = 0.3$ for the broken-power-law model described in Méndez et al. (2002), Makarov et al. (2006), and Li et al. (2022). The vertical red lines mark the location of the TRGB in each subplot.

Inverse variance weighting:

$$\mathrm{EDR}(i) = \frac{N(i+1) - N(i-1)}{N(i+1) + N(i-1)}. \tag{B2}$$

No weighting:

$$\mathrm{EDR}(i) = N(i+1) - N(i-1). \tag{B3}$$

We note that the S/N EDR in Equation (B1) is different than that used in Hatt et al. (2017), which applies the S/N as a weight on top of the Sobel filter (see their Section 3.3.2). We plot the EDRs from these variations in Figure 9. We find that adopting different smoothing and weighting can shift the measured TRGB by several hundredths of a magnitude.

To reduce this bias along the distance ladder, we have chosen the EDR in Equation (B1), which has the smallest bias, and we set the smoothing value to be the same in both this calibration for NGC 4258 and application to SN hosts for first-order cancellation. Following the optimal values found in Wu et al. (2023), we use baseline parameters of spatial clipping of 10%, color band of 1 mag, smoothing of 0.1, Sobel threshold fraction of 0.6, and the "error weighting" EDR.

Appendix C
Simulated LF with Different Smoothing

We visualize the effect of smoothing on the measured tip and TCR with Figure 10, where we generate four simulated populations with [Fe/H] = −2.0, −1.67, −1.33, and −1.0 and ages of 13, 9.7, 6.3, and 3 Gyr, respectively. In the CMDs, the blue slanted lines represent the color band optimized with the CATs algorithm, and the histogram in the right panel corresponds to stars within the color band only. The blue and red lines correspond to measurements using smoothing parameters of $s = 0.05$ and 0.15, respectively. Dashed lines correspond to the smoothed LFs, and dotted–dashed lines correspond to the Sobel responses. We add the same 0.05 mag noise to the F814W and F606W magnitudes as described above and measure the "measured" tip using the CATs algorithm. From this plot, we see that increasing smoothing from 0.05 to 0.15 pushes stars fainter than the tip across the tip in the brighter direction by flattening the tip discontinuity. This in turn pushes the measured tip in the brighter direction, as shown by the separation between the red horizontal lines in each subplot.

From Figure 10, we observe that (1) adding noise tends to scatter the tip brightward, as there are more RGB stars that are moved to the region brighter than the tip than vice versa due to the intrinsic relative number of stars in each evolutionary stage; and (2) increasing the smoothing from 0.05 to 0.15 biases the measured tip in the brightward direction. The extra stars that are pushed from the region fainter than the measured tip to the region brighter than the measured tip can be visualized as the shaded red space under the dashed lines in each panel. A larger

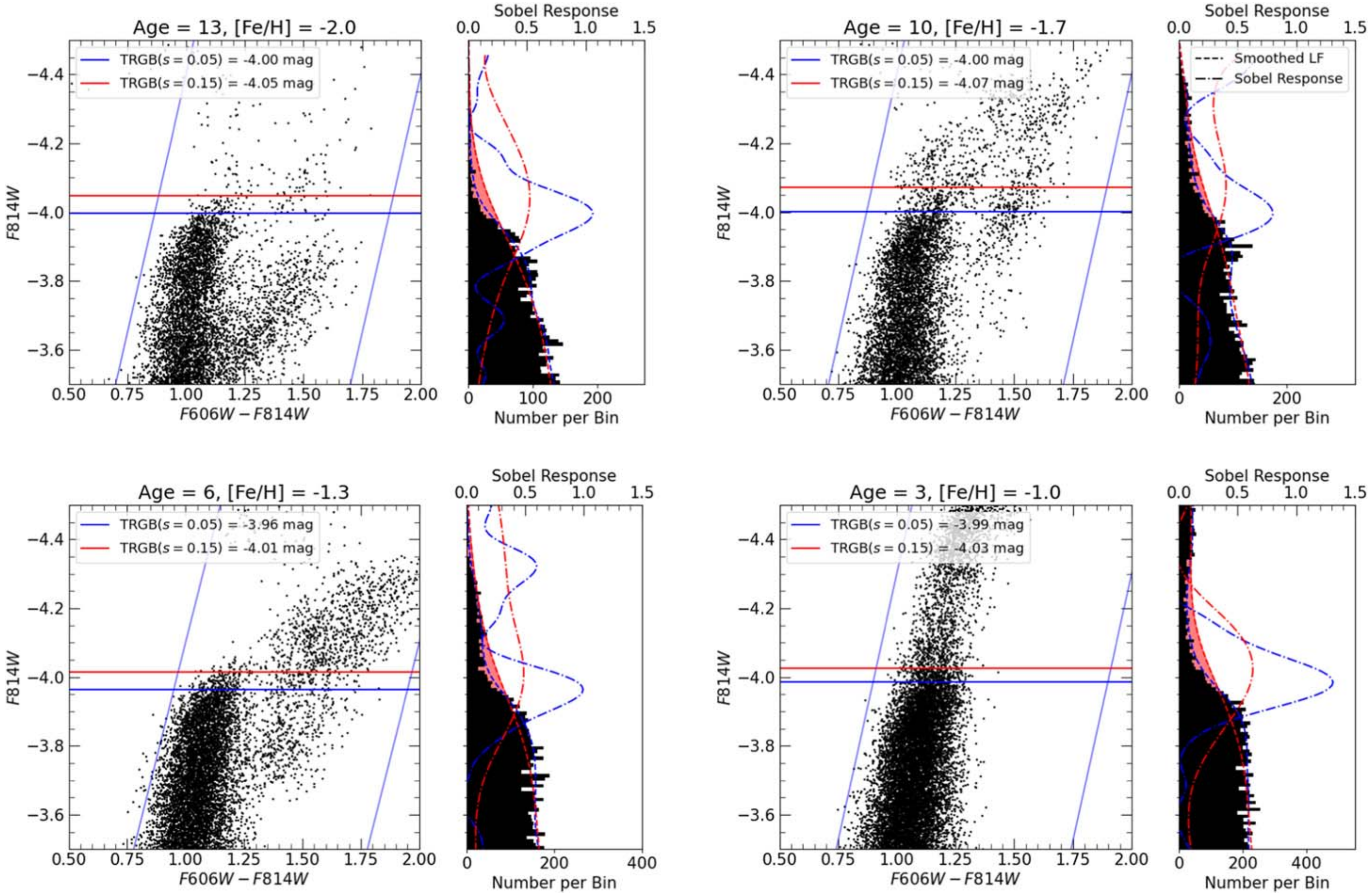

Figure 10. CMDs and LFs for simulated stellar populations of [Fe/H] = −2.0, −1.7, −1.3, and −1.0 and ages of 13, 10, 6, and 3 Gyr, respectively, from clockwise order from the top left. Blue diagonal lines in the left subpanels are the color bands used. Red and blue lines in both subpanels correspond to smoothing values of $s = 0.05$ and $s = 0.15$, respectively. Solid, dashed, and dotted–dashed lines correspond to the measured tip, smoothed LF, and Sobel response, respectively. We shade the extra space representing extra stars underneath the smoothed LF created by applying a higher smoothing parameter in red.

smoothing generates a larger region indicating more stars around the tip are pushed in the brightward direction. This effect is intensified with larger contrast ratios where the tip discontinuity is larger. Smoothing values used by CATs typically do not reach this high, however, we caution that oversmoothing can bias the measured tip in the brightward direction depending on the observed LF (Anderson et al. 2023). This also illustrates the need for applying consistent smoothing for both zero-point and apparent magnitude tip measurements, as different smoothing values will offset the measured tip from the true tip by different amounts due to this effect. A similar effect was found by Anderson et al. (2023) who found a bias that is not necessarily linear and is a function of contrast (with a different definition than that used here) and steepness of the tip discontinuity for a fixed smoothing value. They note that there is often a lack of an objective criterion for choosing the smoothing scale (for instance, Hatt et al. 2017 suggests that one can increase the smoothing scale until there is a single, dominant, local maximum in the Sobel response) and define a criterion such that the choice of smoothing should not change the result more than 0.1 mag/mag. They also note that the smoothing scale should be used consistently in the anchor and SN Ia calibrator galaxies as this bias would otherwise not cancel out.

As the tip is biased in the brighter direction for a given LF, the decrease in the number of AGB stars is greater than the decrease in the number of RGB stars in the 0.5 mag region around the tip. In terms of the broken-power-law model (Méndez et al. 2002; Makarov et al. 2006; Li et al. 2022), the c or γ parameter (AGB slope) is greater than the a or α parameters (RGB slope). As the tip is biased brightward with larger smoothing, R will also change accordingly, given the same LF is used in this comparison. We note this situation, where the LF remains constant but the measured tip changes, is different from the tip–contrast ratio calibration where the population of stars changes for each measurement.

Appendix D
LMC

In this section, we investigate the feasibility of using the tip calibration from Hoyt (2023) for H_0 measurements and whether the TCR is consistent with their findings. Hoyt (2023) measure a subpercent calibration of the tip using red giants in the LMC by selectively removing 15 out of 20 fields on the basis of a subjective evaluation of their Sobel responses and bootstrap asymmetry. We note that the fields Hoyt (2023) removes are systematically fainter, suggesting a relationship between the tip magnitude and the cleanness of the Sobel response.

To see if these same cuts can be feasibly applied to SN Ia hosts, we first apply the CATs algorithm to the SN Ia host galaxies from Scolnic et al. (2023). We perform 10,000 bootstrap resamples for each galaxy and plot the 90% width of the bootstrapped samples in Figure 11. We record only the tip corresponding to the highest Sobel peak.

We find that none of the galaxies would pass the cuts shown in Extended Data Figure 1 shown in Hoyt (2023). In other words, it would not be possible to choose brighter fields in these host galaxies selectively as done in Hoyt (2023) for the LMC. We conclude that the tip calibration from Hoyt (2023) cannot be used to calibrate tip measurements in host galaxies to measure H_0.

Next, we take the same 20 measured tips from Hoyt (2023), which were measured in 20 Voronoi fields based on the concepts from Cappellari & Copin (2003) and Hoyt et al. (2018) and attributed to M. Seibert, and measure their contrast ratios. We plot the tips as a function of their contrast ratio in Figure 12. We see a trend that is indicative of a TCR. We do not plot uncertainties or apply a fit because the errors quoted in Hoyt (2023) do not account for field-to-field dispersion such as

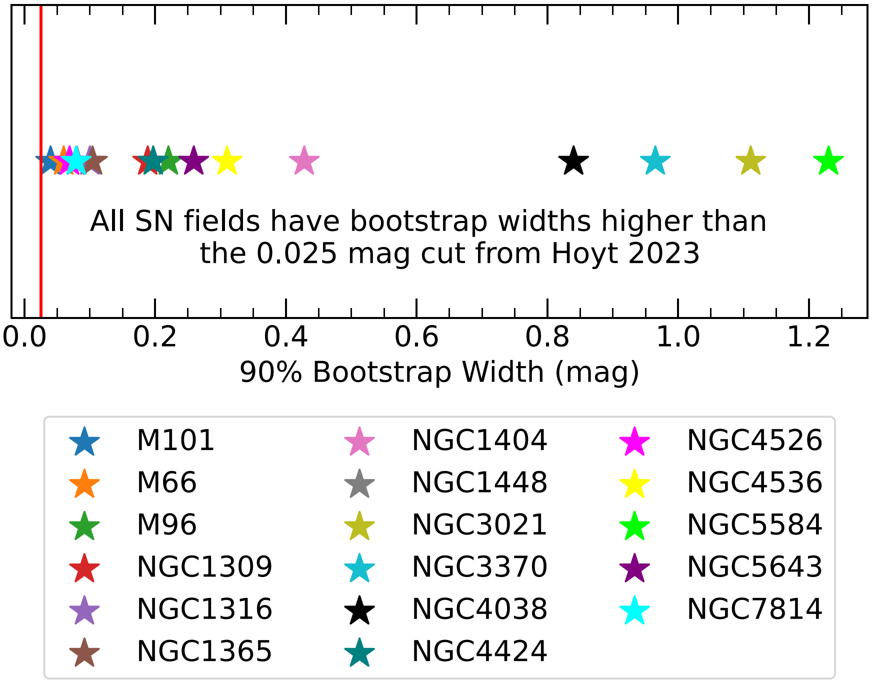

Figure 11. 90% bootstrap widths for the SN Ia host galaxies from Scolnic et al. (2023). We indicate the limit of 0.025 mag used by Hoyt (2023) to select LMC fields such that all bootstrap widths greater than 0.025 mag would be rejected. We find that none of the SN Ia host galaxies would pass the cuts made by Hoyt (2023) for the LMC.

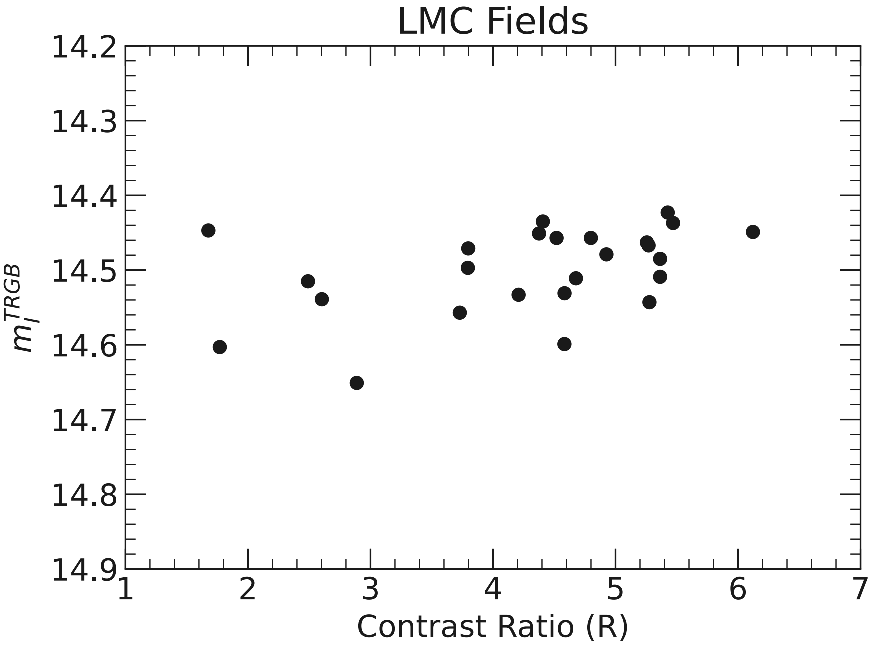

Figure 12. Tips from Hoyt (2023) as a function of their contrast ratio.

the one calibrated in Wu et al. (2023). In addition, the error equation in Equation (1) was calibrated using fainter GHOSTS galaxies and will overestimate the uncertainties for the LMC tips, which are much brighter. We defer a more detailed treatment with the CATs algorithm to future work.

ORCID iDs

Siyang Li https://orcid.org/0000-0002-8623-1082
Adam G. Riess https://orcid.org/0000-0002-6124-1196
Daniel Scolnic https://orcid.org/0000-0002-4934-5849
Gagandeep S. Anand https://orcid.org/0000-0002-5259-2314
Jiaxi Wu https://orcid.org/0000-0003-3829-967X
Wenlong Yuan https://orcid.org/0000-0001-9420-6525
Rachael Beaton https://orcid.org/0000-0002-1691-8217
Richard I. Anderson https://orcid.org/0000-0001-8089-4419

References

Alam, S., Albareti, F. D., Allende Prieto, C., et al. 2015, ApJS, 219, 12
Anand, G. S., Rizzi, L., & Tully, R. B. 2018, AJ, 156, 105
Anand, G. S., Rizzi, L., Tully, R. B., et al. 2021, AJ, 162, 80
Anand, G. S., Tully, R. B., Rizzi, L., Riess, A. G., & Yuan, W. 2022, ApJ, 932, 15
Anderson, R. I. 2022, A&A, 658, A148
Anderson, R. I., Casertano, S., Riess, A., & Spetsieri, Z. 2021, HST Proposal, Cycle 29, 16688
Anderson, R. I., Koblischke, N. W., & Eyer, L. 2023, arXiv:2303.04790
Beaton, R. L., Bono, G., Braga, V. F., et al. 2018, SSRv, 214, 113
Blakeslee, J. P., Jensen, J. B., Ma, C.-P., Milne, P. A., & Greene, J. E. 2021, ApJ, 911, 65
Cappellari, M., & Copin, Y. 2003, MNRAS, 342, 345
Choi, J., Dotter, A., Conroy, C., et al. 2016, ApJ, 823, 102
Condon, J. J. 1987, ApJS, 65, 485
Condon, J. J., Helou, G., Sanders, D. B., & Soifer, B. T. 1996, ApJS, 103, 81
Dolphin, A. 2016, DOLPHOT: Stellar photometry, Astrophysics Source Code Library, ascl:1608.013
Dolphin, A. E. 2002, MNRAS, 332, 91
Dotter, A. 2016, ApJS, 222, 8
Ferrarese, L., Mould, J. R., Kennicutt, R. C., et al. 2000, ApJ, 529, 745
Freedman, W. L. 2021, ApJ, 919, 16
Freedman, W. L., Madore, B. F., Gibson, B. K., et al. 2001, ApJ, 553, 47
Freedman, W. L., Madore, B. F., Hatt, D., et al. 2019, ApJ, 882, 34
Freedman, W. L., Madore, B. F., Hoyt, T., et al. 2020, ApJ, 891, 57
Górski, M., Pietrzyński, G., Gieren, W., et al. 2018, AJ, 156, 278
Greco, J. P., & Danieli, S. 2022, ApJ, 941, 26
Greenhill, L. 2004, HST Proposal, Cycle 13, 10399
Hatt, D., Beaton, R. L., Freedman, W. L., et al. 2017, ApJ, 845, 146
Heald, G., Józsa, G., Serra, P., et al. 2011, A&A, 526, A118
Hislop, L., Mould, J., Schmidt, B., et al. 2011, ApJ, 733, 75
Hoyt, T., Freedman, W. L., Beaton, R. L., et al. 2021, HST Proposal, Cycle 29, 16743
Hoyt, T. J. 2023, NatAs, 7, 590
Hoyt, T. J., Freedman, W. L., Madore, B. F., et al. 2018, ApJ, 858, 12
Jang, I. S., Hoyt, T. J., Beaton, R. L., et al. 2021, ApJ, 906, 125
Jang, I. S., & Lee, M. G. 2015, ApJ, 807, 133
Jang, I. S., & Lee, M. G. 2017, ApJ, 835, 28
Kim, Y. J., Kang, J., Lee, M. G., & Jang, I. S. 2020, ApJ, 905, 104
Lee, M. G., Freedman, W. L., & Madore, B. F. 1993, ApJ, 417, 553
Lee, M. G., & Jang, I. S. 2012, ApJL, 760, L14
Lee, M. G., & Jang, I. S. 2013, ApJ, 773, 13
Li, S., Casertano, S., & Riess, A. G. 2022, ApJ, 939, 96
Madore, B. 2002, HST Proposal, Cycle 11, 9477
Madore, B. F., Mager, V., & Freedman, W. L. 2009, ApJ, 690, 389
Makarov, D., Makarova, L., Rizzi, L., et al. 2006, AJ, 132, 2729
McQuinn, K. B. W., Boyer, M., Skillman, E. D., & Dolphin, A. E. 2019, ApJ, 880, 63
McQuinn, K. B. W., Skillman, E. D., Dolphin, A. E., Berg, D., & Kennicutt, R. 2016, ApJ, 826, 21
McQuinn, K. B. W., Skillman, E. D., Dolphin, A. E., Berg, D., & Kennicutt, R. 2017, AJ, 154, 51
Ménard, B., Scranton, R., Fukugita, M., & Richards, G. 2010, MNRAS, 405, 1025
Méndez, B., Davis, M., Moustakas, J., et al. 2002, AJ, 124, 213
Mould, J., & Sakai, S. 2009, ApJ, 697, 996
Paxton, B., Bildsten, L., Dotter, A., et al. 2011, ApJS, 192, 3
Paxton, B., Cantiello, M., Arras, P., et al. 2013, ApJS, 208, 4
Paxton, B., Marchant, P., Schwab, J., et al. 2015, ApJS, 220, 15
Pesce, D. W., Braatz, J. A., Reid, M. J., et al. 2020, ApJL, 891, L1
Radburn-Smith, D. J., de Jong, R. S., Seth, A. C., et al. 2011, ApJS, 195, 18
Reid, M. J., Pesce, D. W., & Riess, A. G. 2019, ApJL, 886, L27
Riess, A., Casertano, S., Filippenko, A. V., et al. 2020, HST Proposal, Cycle 28, 16198
Rizzi, L., Tully, R. B., Makarov, D., et al. 2007, ApJ, 661, 815
Sakai, S., Madore, B. F., & Freedman, W. L. 1996, ApJ, 461, 713

Schlafly, E. F., & Finkbeiner, D. P. 2011, ApJ, 737, 103
Scolnic, D., Riess, A. G., Wu, J., et al. 2023, ApJL, 954, L31
Serenelli, A., Weiss, A., Cassisi, S., Salaris, M., & Pietrinferni, A. 2017, A&A, 606, A33
Tammann, G. A., & Reindl, B. 2013, A&A, 549, A136
Tammann, G. A., Sandage, A., & Reindl, B. 2008, ApJ, 679, 52
Tully, R. B., Courtois, H. M., Dolphin, A. E., et al. 2013, AJ, 146, 86
Tully, R. B., Rizzi, L., Shaya, E. J., et al. 2009, AJ, 138, 323
Wu, J. 2023, JiaxiWu1018/CATS-H0: v1.0, Zenodo, doi:10.5281/zenodo.8271583
Wu, J., Scolnic, D., Riess, A. G., et al. 2023, ApJ, 954, 87
Wu, P.-F., Tully, R. B., Rizzi, L., et al. 2014, AJ, 148, 7